

Modeling the Photoionized Interface in Blister HII Regions

Ravi Sankrit¹

The Johns Hopkins University

and

J. Jeff Hester²

Arizona State University

ABSTRACT

We present a grid of photoionization models for the emission from photoevaporative interfaces between the ionized gas and molecular cloud in blister H II regions. For the density profiles of the emitting gas in the models, we use a general power law form calculated for photoionized, photoevaporative flows by Bertoldi (1989). We find that the spatial emission line profiles are dependent on the incident flux, the shape of the ionizing continuum and the elemental abundances. In particular, we find that the peak emissivity of the [S II] and [N II] lines are more sensitive to the elemental abundances than are the total line intensities. The diagnostics obtained from the grid of models can be used in conjunction with high spatial resolution data to infer the properties of ionized interfaces in blister H II regions. As an example, we consider a location at the tip of an “elephant trunk” structure in M 16 (the Eagle Nebula) and show how narrow band HST-WFPC2 images constrain the H II region properties. We present a photoionization model that explains the ionization structure and emission from the interface seen in these high spatial resolution data.

Subject headings: H II regions: individual (M 16) — H II regions: photoionization

¹ravi@pha.jhu.edu

²jhester@asu.edu

1. Introduction

A blister H II region is formed when a massive star is born near the edge of a molecular cloud. The radiation from the newborn star rapidly ionizes the surrounding material and the ionization front breaks through the surface of the cloud creating a cavity. The photoionized gas in the cavity is exposed to view and can be observed as a blister on the surface of the molecular cloud. The concept of a blister was introduced by Zuckerman (1973) to describe the Orion Nebula, one of the nearest and definitely the best studied H II region. The term “blister model” was introduced by Israel (1978) who studied a sample of about 30 galactic H II regions and, based on their positional relationship to CO emitting molecular clouds, concluded that almost every optically observable H II region is a blister H II region.

Blister H II regions serve as useful probes of current interstellar abundances in the Galaxy, since the stars responsible for maintaining the ionization are less than about 10 million years old. Classical techniques of nebular analysis (described in several textbooks, such as Aller (1984) and Osterbrock (1989)), based mainly on optical spectra, have been used to determine abundances in several H II regions and map abundances in the Galaxy (e.g. Hawley (1978), Shaver et al. (1983)). These methods have two well known uncertainties. First, lines from all the ionization stages of an element present in an H II region are usually not observed. This requires prescriptions to correct for unseen stages of one element based on ionic ratios of a different element. Second, temperatures derived from lines of one species (such as [O III]) are assumed when obtaining the abundance of another species (such as [S II]) which is formed in a different zone. These uncertainties are discussed by French & Grandi (1981).

An alternative method of determining abundances is by using photoionization models to interpret H II region spectra. This approach has been applied in some detail to the Orion Nebula (Baldwin et al. (1991), Rubin et al. (1991)) and has the advantage that the electron temperature and ionization structure are calculated self-consistently. Furthermore, it becomes unnecessary to implement ad-hoc ionization correction schemes. However a major limitation of this method (as emphasized by Rubin et al. (1998)) is that the input density and geometry need to be specified in order to calculate models, and these in general are not well known.

In a blister H II region, the density profile of the interface between the molecular cloud and the ionized gas is determined by the ionizing radiation driving a photoevaporative flow off the surface of the molecular cloud. The sharply stratified ionization structure of this interface was observed in the Orion Nebula by Hester et al. (1991) in *Hubble Space Telescope* (HST) *Wide Field Camera* narrow band images. The ionization stratification

was discussed in the broader context of interpreting H II region spectra by Hester (1991), who also suggested that most of the [S II] emission arises in a very narrow transition zone between the H II region interior and the photodissociation region of the molecular cloud. The transition zone occurs beyond the hydrogen ionization edge, where photons with energies higher than 10.4 eV (the ionization potential of S⁰) keep the sulphur singly ionized. More recently, Hester et al. (1996) presented HST *Wide Field and Planetary Camera - 2* (WFPC2) images of the “elephant trunk” structures in the blister H II region M 16. In these images, the photoionized interface is seen in tangency and the ionization stratification is clearly resolved. The [S II] emitting zone is very narrow – it has a width of about 8×10^{15} cm ($\lesssim 0\prime.3$ at the assumed distance of 2000 pc). In that work, we used an empirical density profile derived from the H α emission profile and presented a photoionization model that successfully reproduced the main features of the emission from the interface.

In this paper, we use photoionization models in conjunction with high spatial resolution data to develop a framework for interpreting H II region spectra. Arbitrary assumptions about the density structure are not made, since the models are constrained by the structure observed in the high resolution images. Once such a framework is established, it will be a powerful method for obtaining the physical properties of the emitting gas in H II regions.

We first present a grid of models for the interface in blister H II regions using the density profiles calculated by Bertoldi (1989) for photoionized, photoevaporative flows. (These calculations are a significant improvement over earlier work because they allow for an ionization front of finite width, rather than treating it as a discontinuity, and they treat non-equilibrium ionization and energy deposition). We vary the incident stellar continuum, the ionizing flux and the elemental abundances and examine the dependence of nebular properties on these input parameters. We focus on the diagnostics provided by spatially resolved line strengths (such as can be obtained by HST for several nearby H II regions). We then consider the M 16 data in detail and present a photoionization model for the emission. We compare the model results to published spectra and show how knowledge of the structure of the emitting region is crucial for interpreting ground based observations. We conclude with a summary and a consideration of the implications of our work, and future directions.

2. Photoionization Models

2.1. Input Parameters

The basic input parameters for the photoionization models are the shape and intensity of the incident ionizing continuum and the elemental abundances. The interface between the molecular cloud and the H II region interior is the result of a photoevaporative flow driven by the incident stellar continuum (which is also responsible for ionizing the gas). The solutions for such a flow determine the density profile of the interface, which also needs to be specified.

Hydrodynamic models for photoionized, photoevaporative flows off spherical cloud surfaces have been calculated by Bertoldi (1989) and Bertoldi & Draine (1996). The form of the density profile they find may be written as follows:

$$n(x) = n_0 \left(1 + \frac{R-x}{r_c}\right)^{-2.5} \quad (1)$$

Here, x is the distance from the ionizing source, R is the distance from the source to the ionization edge, and n_0 is the number density at $x = R$. (Note that the density is a function of the distance from the interface, $R - x$, and the actual distance from the source is not explicitly required in the models). The radius of curvature of the evaporating surface is given by r_c and is effectively the scale length for the flow. The values of R and n_0 depend on the ionizing continuum. For each of our models (see below), we start by performing a calculation with $R = 5 \times 10^{17}$ cm and $n_0 = 1500$ cm $^{-3}$, and then iterate using the predicted values at the ionization edge till we obtain the correct values. (We found that 3 iterations were sufficient in every case). We keep the value of r_c fixed at 2×10^{17} cm for all the models, anticipating our analysis of the M 16 data in §3.

The validity of using equation 1 for the density profile is subject to the following caveat. The models calculated by Bertoldi (1989) did not include the effects of dust on the flow. It was shown by Baldwin et al. (1991) that grains absorb, and are ionized by the incident continuum and cause a radial acceleration of the gas away from the star. This phenomenon will affect the outer regions of the flow and alter the density profile. In order to assess the effect on the density profile at and near the interface (which we are concerned with here), the hydrodynamic and photoionization problem would have to be solved self consistently, taking into account the presence of dust - a task beyond the scope of this paper.

We calculate a grid of 60 models, using all combinations drawn from 4 stellar atmospheres, 3 values for the ionizing flux and 5 sets of elemental abundances. The stellar atmospheres used are PHOENIX models of B0 ($T_{eff} = 33,340$ K), O8 ($T_{eff} = 38,450$ K), O6 ($T_{eff} = 43,560$ K), and O4 ($T_{eff} = 48,670$ K) stars, all with gravities, $\log(g) = 3.9$ (Hauschildt, Baron & Allard (1997), Aufdenberg, private communication). PHOENIX models represent an advance over earlier model stellar atmospheres since they use spherical

geometry, calculate the strongest lines of important elements in non-LTE, and include line blanketing. In Figure 1 these model spectra are plotted, normalized to their respective peak values. Also shown on the plot are the ionization potentials of S^0 (10.36 eV) and O^+ (35.1 eV). The values used for the incident ionizing flux are $\log [\Phi(H)] = 10.5, 11.0$ and 11.5 , where $\Phi(H)$ is the number of ionizing photons (energy ≥ 13.6 eV) per second per cm^2 incident on the gas. In all the models we keep the helium abundance at solar. The heavier element abundances are varied simultaneously and values of 0.2, 0.4, 0.6, 0.8 and 1.0 times solar (where solar values are taken from Grevesse & Anders (1989)) are used in the grid of models. We use the publicly available code, CLOUDY (Ferland et al. (1998)) to calculate the photoionization models.

One concern about the modeling procedure is that we are using an equilibrium code (CLOUDY) to model the emission from a photoevaporative flow where non-equilibrium effects may be important. At the interface, the cooling times are short (a few tens of years) compared to the dynamic time scales (a few thousand years), so thermal equilibrium is a valid assumption. However sufficiently close to the ionization front, photoionization equilibrium will not hold. The effect of non-equilibrium on the predicted emission lines was studied by Harrington (1977). He found that the ionization fraction differed only moderately between equilibrium and non-equilibrium models, and that happened within about 10^{15} cm of the front. He also found that the lines strengths most affected were $[N\text{ I}] \lambda 5199$ and $[O\text{ I}] \lambda 6300$ which varied about 40% and 15% respectively. Both these lines are formed beyond and are narrower than the $[S\text{ II}]$ zone. While it would be useful to examine the effect of photoionization non-equilibrium in detail for a wider range of conditions than was done by Harrington (1977), we expect our models to be suitable representation of reality.

2.2. Results

The photoionization models predict the highly stratified ionization structure of the interface. The $H\alpha$ more or less follows the density profile as expected. The $[S\text{ II}]$ comes from a narrow zone near the interface that peaks sharply just beyond the $H\alpha$ peak, in a region where the ionization fraction of hydrogen is rapidly falling and sulphur (whose ionization potential is lower than hydrogen) is kept singly ionized. The $[O\text{ III}]$ emission profile is always less peaked and often quite extended compared to the $H\alpha$ and $[S\text{ II}]$. While all models show these general characteristics of the low ionization and high ionization gas, there are significant differences in the details of the spatial profiles and line strengths among the various models. We now turn to a discussion of these differences and their dependence

on input parameters.

In Figure 2 we show the density and the $H\alpha$, [S II] $\lambda\lambda 6716, 6731$ and [O III] $\lambda 5007$ emissivity as a function of distance from the interface for two models. Both models use an O6 star continuum and abundances of 0.6 solar for elements heavier than helium. The models shown differ in the incident ionizing fluxes – $\Phi_H = 10^{10.5}$ photons $s^{-1} \text{ cm}^{-2}$ (top panel) and $\Phi_H = 10^{11.5}$ photons $s^{-1} \text{ cm}^{-2}$ (bottom panel). The most dramatic difference between the two models is the density at the ionization front, which is about 3 times higher for the higher incident flux. Consequently the peak $H\alpha$ emission is higher by about a factor of 10 (since emissivity is proportional to the square of the density). This is a result of the ionization front being pushed into a cloud where the density increases towards the interior – a larger flux of ionizing photons will push the front further up the density ramp. The [S II] and [O III] emissivities are also correspondingly higher.

In both plots of Figure 2, the origin of the x-axis is chosen to be at the peak of the [S II] emission. We can see from these plots, that the width of the [S II] zone varies considerably with changes in the incident ionizing flux. If we define the width as being the distance at which the [S II] emissivity falls to half its peak value, then the widths for the two cases shown are 11.2×10^{15} cm for the lower ionizing flux (top panel) and 4.4×10^{15} cm for the higher ionizing flux (bottom panel). At a distance of 1 kpc, these widths correspond to $0''.75$ and $0''.29$ respectively.

In Figure 3, models with different shapes for the incident continuum are shown. The top and bottom panels show models using O8 and O4 stellar atmospheres. Both models use an incident ionizing flux of $10^{11.0}$ photons $s^{-1} \text{ cm}^{-2}$ and metal abundances of 0.6 times solar. The [O III] emission is higher by a factor of about 6 for the O4 model while $H\alpha$ and [S II] are about the same. This is because the fraction of photons produced which are capable of ionizing oxygen to O^{++} is much lower for O8 stars than for O4 stars (Figure 1). Here again, the [S II] profiles are significantly different. The O8 star produces an [S II] zone that is $\sim 12.3 \times 10^{15}$ cm wide (top panel) and the hotter O4 star produces a narrower [S II] zone ($\sim 6.4 \times 10^{15}$ cm).

The variation of emission profiles with abundance is shown in Figure 4. Both models use an O6 stellar atmosphere and an ionizing flux of $10^{11.0}$ photons $s^{-1} \text{ cm}^{-2}$. The models shown in the top and bottom panels have the abundances of all elements heavier than helium set to 0.2 times solar and 0.8 times solar respectively. The $H\alpha$ intensity is about the same in both cases, and the total [S II] intensity is 1.6 times higher in the model with the higher abundance. The ratio of the peak [S II] emissivity to the peak $H\alpha$ emissivity shows a stronger contrast between the models. In the case of the low abundance model this ratio is 0.27, while for the high abundance model it is 0.55, which is a factor of 2 higher.

2.2.1. *Stellar Atmosphere Models*

The spectral energy distribution of the incident ionizing continuum is a key ingredient in HII region models. Since the ionizing photons cannot be observed for any but a handful of stars, we depend on continua predicted by theoretically computed stellar atmospheres. In this paper we are using atmospheres calculated by the PHOENIX code, which treats the atmosphere as spherically symmetric, includes line blanketing, and treats the strongest lines of several important elements in non-LTE. These models are an improvement over the widely used ATLAS models (Kurucz (1991)) which are plane-parallel and neglect non-LTE effects entirely.

Another set of theoretical non-LTE stellar atmospheres, the CoStar Models (Schaerer & de Koter (1997)) have also been used recently in H II region models (Stasińska & Schaerer (1997)). CoStar and PHOENIX models differ in significant ways. CoStar models include the effects of stellar winds on the emitted continuum, while the PHOENIX models are spherically extended but hydrostatic atmospheres. However, CoStar models do not include line blanketing in the calculation of the temperature structure whereas PHOENIX models include line blanketing in a self consistent way in determining the temperature structure of the atmosphere. Furthermore CoStar models treat only H and He in non-LTE while PHOENIX treats over 50,000 of the strongest lines of several elements in non-LTE. In this section, we examine the effect of using different model atmospheres on the predicted H II region photoionization model.

Figure 5 shows the spectral energy distributions of the PHOENIX O4V model ($T_* = 48670$ K) and the CoStar E2 model ($T_* = 48500$ K). Also shown are the S^0 and O^{++} ionization edges. The CoStar spectrum is flatter and has a greater flux at higher energies than the PHOENIX spectrum. This effect is due to the wind and is seen in Stasińska & Schaerer (1997) where CoStar and ATLAS spectra are compared. In order to understand the effects of using different stellar atmospheres on H II region spectra, we calculated a photoionization model using the CoStar spectrum along with an incident ionizing flux of $10^{11.0}$ photons $s^{-1} cm^{-2}$, and metal abundances of 0.6 times solar. In Figure 6 we compare this CoStar model with a model using the PHOENIX O4V ionizing continuum with the same incident flux and abundances. The difference between these models is significant - the CoStar continuum produces twice as much [O III] as the PHOENIX continuum. The CoStar model also produces more [S II] and has a somewhat broader [S II] zone. The peak $H\alpha$ is lower in the CoStar model, so the peak [S II] to peak $H\alpha$ is higher by a factor of 2 compared to the PHOENIX model.

We wish to caution the reader that currently it is very uncertain as to which of these models (PHOENIX or CoStar) is closer to reality. However our comparison has shown that

in their current forms, the ionizing continua from by PHOENIX and CoStar predict very different H II region line strengths. A thorough understanding of H II region spectra can be of value in validating atmosphere models as pointed out by Rubin, Kunze, & Yamamoto (1995). It is beyond the scope of this work to pursue this issue further and for the rest of the paper, we will discuss models using only PHOENIX stellar continua.

2.3. Diagnostics

The grid of models we have calculated predict several quantities that could serve as useful starting points in analyzing spectra of blister H II regions, particularly for the cases where the emitting interface is spatially resolved. We now present and discuss some of these diagnostics.

In most of the following plots, we will be visualizing the data in a somewhat specialized way which is worth describing here. The quantity of interest is plotted on the y-axis. The x-axis is simply the model number (from 1 to 60, with the tick marks suppressed). The 4 large divisions in the plot correspond to stellar atmospheres used in the model (models 1 through 15 use a B0 atmosphere and so on). Within each set of 15 models, groups of 5 (differentiated by the symbols used) correspond to different values for the ionizing flux. Finally, within each group of 5, the heavy element abundances go from 0.2 solar to 1.0 solar in steps of 0.2 with increasing model number.

In the top panel of Figure 7 we show the maximum density reached in each model. This is the hydrogen density at the ionization edge defined (for convenience) to be the point where n_e/n_H has fallen below 0.001. (We note, however that the observed lines are not emitted so far into the photodissociation region – for instance, the [S II] peak occurs where $n_e \sim 0.7n_H$). The density at the ionization edge depends strongly on the ionizing flux (for the reason mentioned in the previous section). There is, however no dependence on the stellar temperature; (note that the four large divisions in the plot correspond to different ionizing stars). For higher incident flux, there is a noticeable dependence on the abundance. A higher abundance of metals implies that more atoms compete for the ionizing photons and the maximum density reached is lower. The peak $H\alpha$ emission depends on the density at the ionization edge. The bottom panel of Figure 7 is a scatter plot of the peak $H\alpha$ against the maximum density reached in the models. As expected there is a strong correlation between the $H\alpha$ peak emissivity and the maximum density. This in turn implies that the peak $H\alpha$ emissivity is a good discriminant for the incident ionizing flux.

Next, we discuss the peak emissivities and total line intensities of three important

diagnostic lines in H II regions – [O III] $\lambda 5007$, [S II] $\lambda\lambda 6716, 6731$ and [N II] $\lambda 6584$. In what follows, all peak emissivities and total intensities are taken relative to $H\alpha$, and this is to be understood even if not explicitly mentioned. Note that the peak emissivity for different lines occurs at different locations.

Figure 8 shows plots of the peak [O III] emissivity (top panel) and the total [O III] intensity (bottom panel) for the grid of models. Both these quantities are most sensitive to the stellar type. [O III] $\lambda 5007$ is a high ionization line and in spectra of H II regions, it is an indicator of the hardness of the ionizing spectrum. For a given ionizing flux, either the peak [O III] emissivity or the total [O III] intensity could be used to distinguish the shape of the incident ionizing continuum. For models using a given star type and ionizing flux, the [O III] peak emissivity and intensities reach a maximum for abundances about 0.4 solar. The decrease in emission for lower abundances is simply because there is less oxygen. For higher abundances, the increased oxygen abundance leads to the [O III] $52 \mu\text{m}$ and $88 \mu\text{m}$ infrared lines dominating the cooling and lowering the electron temperature of the gas (see e.g. Henry (1993)). At lower temperatures the intensity of [O III], a collisionally excited line, decreases.

In contrast to [O III], the [S II] $6716, 6731 \text{ \AA}$ lines trace low ionization gas. These [S II] lines are the only strong optical lines for any ionization stage of sulphur and are therefore have been of great importance in estimating S abundances in nebulae. However the dominant state of sulphur in most H II regions is S^{++} and obtaining only the S^+ abundance leads to large uncertainties in the total sulphur abundance estimates (e.g. Dennefeld & Stasińska (1983)). In Figure 9 we show plots of the peak [S II] emissivity (top panel) and the total [S II] intensity (bottom panel) for the grid of models. (Note that the y-axis scales are different on the two plots). For models with the same ionizing continuum and flux, the peak [S II] emissivity is more sensitive than the total [S II] intensity to changes in abundance, at least for lower abundances. The sensitivity gets better when the ionizing continuum is from hotter stars (O4 and O6 in our grid). Conversely, the peak [S II] is less sensitive than the total [S II] intensity to the incident ionizing flux. (Both quantities decrease with increased ionizing flux). Therefore, with spatially resolved data for an H II region interface, the peak [S II] emissivity can be used to estimate the sulphur abundance.

The ionization potential of N^0 is 14.5 eV, somewhat higher than that of hydrogen. In addition to direct ionization from the ground state, N^0 in the excited 2D state can be ionized by photons below the Lyman limit, and in some cases the latter may dominate the ionization balance, and affect the [N II] emission lines. However in all our models, the [N II] $\lambda 6584$ emission arises in between the [S II] zone and the [O III] zone and can be considered a tracer of intermediate ionization gas. The strength of this line is generally

used to estimate the abundance of N^+ and via the use of an ionization correction factor, the total nitrogen abundance as well (e.g. Mathis (1982)). Figure 10 shows the peak [N II] emissivity (top panel) and the total [N II] intensity (bottom panel) for the grid of models. As was the case for [S II], these plots show that the peak [N II] is more sensitive indicator of abundance than the total intensity. For models using O8, O6 and O4 stellar continua, the [N II] intensity decreases with increasing flux. Also, the [N II] intensity decreases for hotter ionizing stars. The reason is that in both these cases more nitrogen gets ionized to N^{++} due to the larger number of energetic photons. However, the peak emissivity depends on the N^+ density in the zone where the emission actually reaches its maximum. This ion density is proportional to the total density, which increases with increasing ionizing flux. The peak [N II] emissivity is therefore higher for greater ionizing flux and for hotter stars.

We have presented a grid of models and discussed the results and diagnostics obtained from them. We now consider the specific case of the blister H II region M 16 as an example of how these model results can be applied.

3. The Blister H II Region M 16

HST-WFPC2 images of three elephant trunk structures in M 16 have been presented and discussed in detail by Hester et al. (1996). Figure 11 shows the Planetary Camera image of the head of the second column. The images have a resolution of $0''.046$, corresponding to a linear distance of 1.35×10^{15} cm at an assumed distance of 2000 pc (e.g. Hillenbrand et al. (1993)). The $H\alpha$ and [S II] images show the ionized interface between the opaque molecular cloud and the H II region. Striations in the $H\alpha$ image are due to emission from the photoevaporated gas streaming away from the molecular cloud surface. The [O III] emission is much more extended than the $H\alpha$ and [S II] emission. The ratio map of [S II] to $H\alpha$ peaks around the edge of the column. While it may not be obvious from the image, the ratio along most of the interface is more or less uniform.

For our analysis and modeling, we will concentrate on the emission along a spatial cut across the interface at the tip of the column. The location is shown in the [S II] image in Figure 11. Line flux profiles were taken along the cut, and averaged over a width of 5 pixels. Background intensities were subtracted off, and in addition the [O III] profile was smoothed to remove noise. We note that the background intensity is mainly due to the back wall of the cavity with some contribution from the outer parts of the photoevaporative flow. Here we are concentrating on emission from a narrow region around the interface itself. Plots of the $H\alpha$, [S II] and [O III] intensity profiles are shown in Figure 12 (top panel). The intensities shown in these plots are reddening corrected, taking $E_{B-V} = 0.7$ (Chini & Krügel

(1983)) and the ratio of total to selective extinction, $R = 3.1$, the standard value. For the photoionization model, we assume that the density profile for the emitting gas is given by equation 1 and from Figure 11, we find the radius of curvature, r_c to be 2×10^{17} cm.

The peak $H\alpha$ surface brightness is about 5.5×10^{-13} erg s $^{-1}$ cm $^{-2}$ arcsec $^{-2}$. From the observed geometry (see Figure 11) we estimate that the path length through the emitting region lies between about 6.0×10^{16} cm and 7.5×10^{16} cm. These values give a peak $H\alpha$ emissivity lying between about 4×10^{-18} ergs s $^{-1}$ cm $^{-3}$ and 5×10^{-18} ergs s $^{-1}$ cm $^{-3}$. The conversion of observed to intrinsic flux depends on the extinction. For M 16, Chini & Krügel (1983) have reported that R may be as high as 4.7 (rather than the standard value of 3.1 which we have so far assumed). In that case, the $H\alpha$ emissivity is much higher. Therefore, from Figure 7 we estimate that the observed $H\alpha$ emission requires the density at the interface $n_H \gtrsim 4000$ cm $^{-3}$ and correspondingly an incident ionizing flux $\Phi_H > 10^{11.0}$ photons s $^{-1}$ cm $^{-2}$.

The observed [O III] emission is weak relative to the $H\alpha$ emission (Figure 12, top panel). By integrating the observed profiles out to a distance of about 2×10^{17} cm, we estimate that the total [O III] intensity is 0.7 times the $H\alpha$ intensity. The ionizing flux from stars hotter than O6 or cooler than O8 cannot produce this ratio (Figure 8, bottom panel). The ratio of the peak [S II] emissivity to the peak $H\alpha$ emissivity is between 0.2 and 0.3 (Figure 12, top panel). From our diagnostic plot (top panel of Figure 9), this implies a sulphur abundance lower than about 0.4 solar. Our grid of models uses abundance sets where all the elements heavier than helium vary in lock-step. This is a simplification. For modeling the interface in M 16 we fixed all abundances (except for sulphur) based on the values reported by Hawley (1978), Shaver et al. (1983) and Dennefeld & Stasińska (1983). These values are – helium solar; nitrogen 0.5 times solar; oxygen and the other metals 0.8 times solar. The sulphur abundance was allowed to vary.

The $H\alpha$, [S II] and [O III] profiles, along with the density profile for our final M 16 model are presented in the bottom panel of Figure 12. The ionizing continuum used in the model is from an O7Ia supergiant, with $T_{eff} = 38720$ K and the ionizing flux at the interface is 3×10^{11} photons s $^{-1}$ cm $^{-2}$. The sulphur abundance is 0.4 times solar. The photoionization model reproduces the observed emission from the interface, including the stratified ionization structure of the flow. In matching the model to the observation, we have assumed a plane-parallel geometry – clearly reality is more complex (indeed we have assumed a scale length for the flow based on the radius of curvature of the column). However since we are concentrating on the emission from close to the interface, for our purposes the plane parallel approximation is sufficient.

In Table 1 we present the observed (reddening-corrected) spectrum of M 16 measured

by Hawley (1978) along with the spectrum predicted by our final model. All intensities are given relative to $H\alpha = 100$. The two observed spectra were taken along slits $2''.4$ by $4''.0$ separated by $35''$ along an east-west line in a region at the top of column 1 of the HST image presented by Hester et al. (1996). The spectra at the observed positions vary significantly. The $[S\ II]\ \lambda\lambda\ 6716,6731$ for example is higher by a factor of 4 at position 2. The $[O\ III]\ \lambda 5007$ on the contrary is lower by a factor of $2/3$. Our model spectrum matches the position 1 spectrum rather well. The major exception is the $[O\ II]\ \lambda 3727$ line, where the mismatch may be due to a repositioning error since the $[O\ II]$ line was taken through a separate grating (see Hawley (1978)). Another difference is in the ratio between the two $[S\ II]$ lines. Since the exact location of the observed spectrum is not known and since the observation and model pertain to two different regions (columns 1 and 2 respectively), the reason for the difference is not clear. The total strength of the two lines (relative to $H\alpha$) however is reproduced by the model. It is well known that spectra vary within an H II region. The significance here is that our model matches one of the spectra so well. This allows us to infer that the major reason for the differences in the two observed spectra are due to different orientations of the slit with respect to the highly stratified emitting interface.

4. Concluding Remarks

In this work, we have presented photoionization models for the emission from the photoevaporative interface between the ionized gas and the molecular cloud in blister H II regions. The density profile of the interface is a power-law which can be parameterized by the distance from the ionizing source to the ionization front and the density at the ionization front (Bertoldi & Draine (1996)). The values of these parameters depend upon the shape and strength of the ionizing continuum.

From the grid of models, which have systematically varying input parameters, we find that the $H\alpha$ peak emissivity is strongly dependent on the incident ionizing flux, increasing for higher values of flux. We also find that the $[O\ III]$ emission is most sensitive to the type of star responsible for ionizing the interface. Stars cooler than O8 produce photoionized interfaces with virtually no $[O\ III]$ emission. The low ionization $[S\ II]$ emission is confined to a very sharp zone. We find that the peak $[S\ II]$ emissivity is more sensitive than the total $[S\ II]$ intensity to the sulphur abundance. The same holds true for the intermediate ionization $[N\ II]$ line. It is worth noting that in the $[S\ II]$ zone, the $[S\ II]\ \lambda\lambda 6716,6731$ to $H\alpha$ ratio can get relatively high (e.g. it is > 0.5 for the model shown in the bottom panel of Figure 3). Such high ratios are often considered to be a signature of shock-excited gas but

our models show that they can also occur in photoionized interfaces.

We then considered narrow band HST data of the blister H II region M 16. The emission and ionization structure seen at high resolution was used to constrain the properties of the ionizing continuum and the sulphur abundance. We presented a specific model that reproduced the observations in detail. We found that the integrated spectrum predicted by the model matched one of two ground based spectra taken by Hawley (1978) at a nearby location. These data also validate our photoionization models. Our being able to match the observed emission and ionization structure with these models is strong evidence that blister H II regions can be described by a photoionized, photoevaporative flow.

The method we have presented here is important for the study of H II regions, both in our Galaxy and in other galaxies. In the case of sufficiently nearby objects (such as M 16) we can obtain spatially resolved spectra. Then, our current study indicates that we could use photoionization modeling to obtain elemental abundances without having to make assumptions about the structure of the emitting region. Carrying out such an exercise for a large sample of H II regions will be a crucial test for the applicability of the model for a range of conditions. We can apply our understanding of the emission from nearby H II regions to more distant H II regions (governed by the same physical mechanisms). Specifically, we can calculate photoionization models of photoevaporative flows in order to interpret spectra of these objects. One important class of distant emission nebulae which we may be able to study within this framework are the giant extra-galactic H II regions (GEHRs). It is promising that narrow band HST images of 30 Doradus, the nearest GEHR, show the optical emission concentrated in sharp photoevaporative interfaces, much like in M 16 (Scowen et al. (1998)). A direct application of our method to study the conditions in 30 Doradus would be an important step towards extrapolating to GEHRs in other galaxies.

RS thanks Jason Aufdenberg for discussions about stellar atmospheres and for providing the PHOENIX models used in our calculations. We thank the anonymous referee for several useful comments. Part of this work was completed while RS was a graduate student at Arizona State University. This work was partly supported by NASA/JPL contracts 959289 and 959329.

REFERENCES

- Aller, L. H. 1984, *Physics of Thermal Gaseous Nebulae*, (Dordrecht: Reidel.)
- Baldwin, J. A., Ferland, G. J., Martin, P. G., Corbin, M. R., Cota, S. A., Peterson, B. M., & Slettebak, A. 1991, *ApJ*, 374, 580
- Bertoldi, F. 1989, *ApJ*, 346, 735
- Bertoldi, F. & Draine, B. T. 1996, *ApJ*, 458, 222
- Chini, R. & Krügel, E. 1983, *A&A*, 117, 289
- Dennefeld, M. & Stasińska, G. 1983, *A&A*, 118, 234
- Ferland, G. J., Korista, K. T., Verner, D. A., Ferguson, J. W., Kingdon, J. B., & Verner, E. M. 1998, *PASP*, 110, 761
- French, H. B., & Grandi, S. A. 1981, *ApJ*, 244, 493
- Grevesse, N. & Anders, E. 1989, *Cosmic Abundances of Matter*, AIP Conf. Proc. 183, 1 Ed. C. J. Waddington, (New York: AIP)
- Harrington, J. P. 1977, *MNRAS*, 179, 63
- Hauschildt, P. H., Baron, E. & Allard, F. 1997, *ApJ*, 483, 390
- Hawley, S. A. 1978, *ApJ*, 224, 417
- Henry, R. B. C. 1993, *MNRAS*, 261, 306
- Hester, J. J. 1991, *PASP*, 103, 853
- Hester, J. J. et al. 1991, *ApJ*, 369, L75
- Hester, J. J. et al. 1996, *AJ*, 111, 2349
- Hillenbrand, L. A. et al. 1993, *AJ*, 106, 1906
- Israel, F. P. 1978, *A&A*, 70, 769
- Kurucz, R. L. 1991, in *Stellar Atmospheres: Beyond Classical Models*, NATO ASI Series C, Vol. 341, eds. L. Crivellari, I. Hubeny, D. G. Hummer, page 441
- Mathis, J. S. 1982, *ApJ*, 261, 195

- Osterbrock, D. E. 1989, *Astrophysics of Gaseous Nebulae and Active Galactic Nuclei*, (California: University Science Books)
- Rubin, R. H., Simpson, J. P., Haas, M. R., & Erickson, E. F. 1991, *ApJ*, 374, 564
- Rubin, R. H., Kunze, D., & Yamamoto, T. 1995, in *Astrophysical Applications of Powerful New Atomic Databases*, ASP Conference Proceedings 78, eds. S. J. Adelman, & W. L. Wiese page 479
- Rubin, R. H., Martin, P. G., Dufour, R. J., Ferland, G. J., Baldwin, J. A., Hester, J. J., & Walter, D. K. 1998, *ApJ*, 495, 891
- Schaerer, D. & de Koter, A. 1997, *A&A*, 322, 598
- Scowen, P. A. et al., 1998, *AJ*, 116, 163
- Shaver, P. A., McGee, R. X., Newton, L. M., Danks, A. C., & Pottasch, S. R. 1983, *MNRAS*, 204, 53
- Stasińska, G. & Schaerer, D. 1997, *A&A*, 322, 615
- Zuckerman, B. 1973, *ApJ*, 183, 863

Fig. 1.— The plot shows the PHOENIX model spectra of B0, O8, O6 and O4 stars. These have been used as incident continua in the grid of models presented here. The ionization potentials for S^0 and O^+ are shown. The edge in each of the spectra is at 13.6 eV, corresponding to the ionization potential for H^0 . Note that the fraction of photons with energies greater than 35.12 eV decreases with increasing stellar temperature, while the fraction of photons with energies between 10.4 eV and 13.6 eV increases.

Fig. 2.— Each plot shows model predictions of spatial profiles of the density, and the $H\alpha$, [S II] and [O III] emission. The input parameters for the two models shown differ only in the incident ionizing flux, Φ_H , values of which are shown on the plots. The model with the higher incident flux (bottom panel) leads to a higher density at the interface, correspondingly stronger line fluxes and a narrower [S II] emission zone.

Fig. 3.— Plots are shown as in Figure 2 for models differing in the ionizing stellar atmosphere used. The hotter star (bottom panel) leads to significantly higher [O III] emission and also a narrower [S II] emitting zone.

Fig. 4.— Plots are shown as in Figure 2 for models with different elemental abundances. The increased sulphur abundance leads not only to a higher [S II] line intensity, but also a greater contrast in the ratio of peak [S II] emissivity to the peak $H\alpha$ emissivity.

Fig. 5.— The plot compares the PHOENIX O4V ($T_{eff} = 48,670$ K) spectrum with the CoStar E2 ($T_{eff} = 48,500$ K) spectrum spectrum. The ionization potentials for S^0 and O^+ are shown. The CoStar model includes the effects of a wind which results in a flatter spectrum and consequently a higher fraction of photons able to produce O^{++} .

Fig. 6.— Plots are shown as in Figure 2 for models using PHOENIX and CoStar incident spectra. The incident ionizing flux and abundances are the same for both models. The main difference is that the CoStar model predicts twice as much [O III] as the PHOENIX model.

Fig. 7.— Top Panel: The plot shows the densities at the ionization edge for the grid of models. Different symbols stand for models with different ionizing flux. The plot is divided into four broad regions along the x-axis, each with models using a particular stellar ionizing continuum. Within each group of five consecutive models, the abundance of metals heavier than helium varies from 0.2 to 1.0 in steps of 0.2 going from left to right. The strong dependence of maximum density reached on incident ionizing flux is clearly seen. (The organization of this plot is used for the plots shown in Figures 8, 9 and 10). Bottom Panel: The scatter plot of peak $H\alpha$ emissivity vs. maximum density reached shows the strong correlation between these two quantities. The maximum density in turn is most sensitive to the ionizing flux.

Fig. 8.— The peak [O III] emissivity and the total [O III] intensities for the grid of models are shown in the top and bottom panels respectively.

Fig. 9.— The peak [S II] emissivity and total [S II] intensities for the grid of models are shown in the top and bottom panels. For a given ionizing continuum, the peak emissivity is a much more sensitive indicator of abundance than the total intensity.

Fig. 10.— The peak [N II] emissivity and total [N II] intensities for the grid of models are shown in the top and bottom panels. As in the case of [S II], the peak emissivities are more sensitive indicators of abundance than total intensities.

Fig. 11.— HST images of the top of a “pillar” in M 16 showing the field of view of the PC. The brightened rim around the column is seen clearly in the $H\alpha$ and [S II] images, and also stands out in the [S II] to $H\alpha$ ratio map. The ratio is more or less uniform all around the edge. The ionizing stars lie directly above the tip of the column. The location of the cut across the interface for which emission profiles have been analyzed is shown in the [S II] image.

Fig. 12.— Top Panel: The observed profile across the photoionized interface. The [O III] profile has been smoothed for clarity. The distance scale assumes a distance of 2000 pc to the nebula, and the peak of the [S II] emission lies at 0. Bottom Panel: The emission profiles predicted by the photoionization model. The observed intensity is directly proportional to the model emissivity so the two plots can be directly compared. The density profile used in the model is also shown.

Table 1. Model line strengths compared with observations.

| Line | λ | Pos. 1 | Pos. 2 | Model |
|------------|-----------|--------|--------|-------|
| H α | 6563 | 100.0 | 100.0 | 100.0 |
| He I | 5876 | 4.1 | 6.3 | 4.7 |
| [N II] | 5755 | 0.1 | 0.8 | 0.2 |
| [N II] | 6548 | 5.7 | 17.5 | 7.6 |
| [N II] | 6584 | 18.2 | 55.4 | 22.5 |
| [O II] | 3727 | 56.1 | 114.6 | 109.3 |
| [O III] | 4363 | <1.4 | <1.5 | 0.2 |
| [O III] | 4959 | 16.4 | 9.8 | 22.8 |
| [O III] | 5007 | 50.5 | 32.3 | 66.0 |
| [S II] | 6716 | 2.8 | 8.0 | 2.1 |
| [S II] | 6731 | 2.6 | 10.5 | 3.4 |
| [S III] | 6312 | <0.1 | 0.8 | 0.3 |

Note. — The observed values are taken from Hawley (1978)

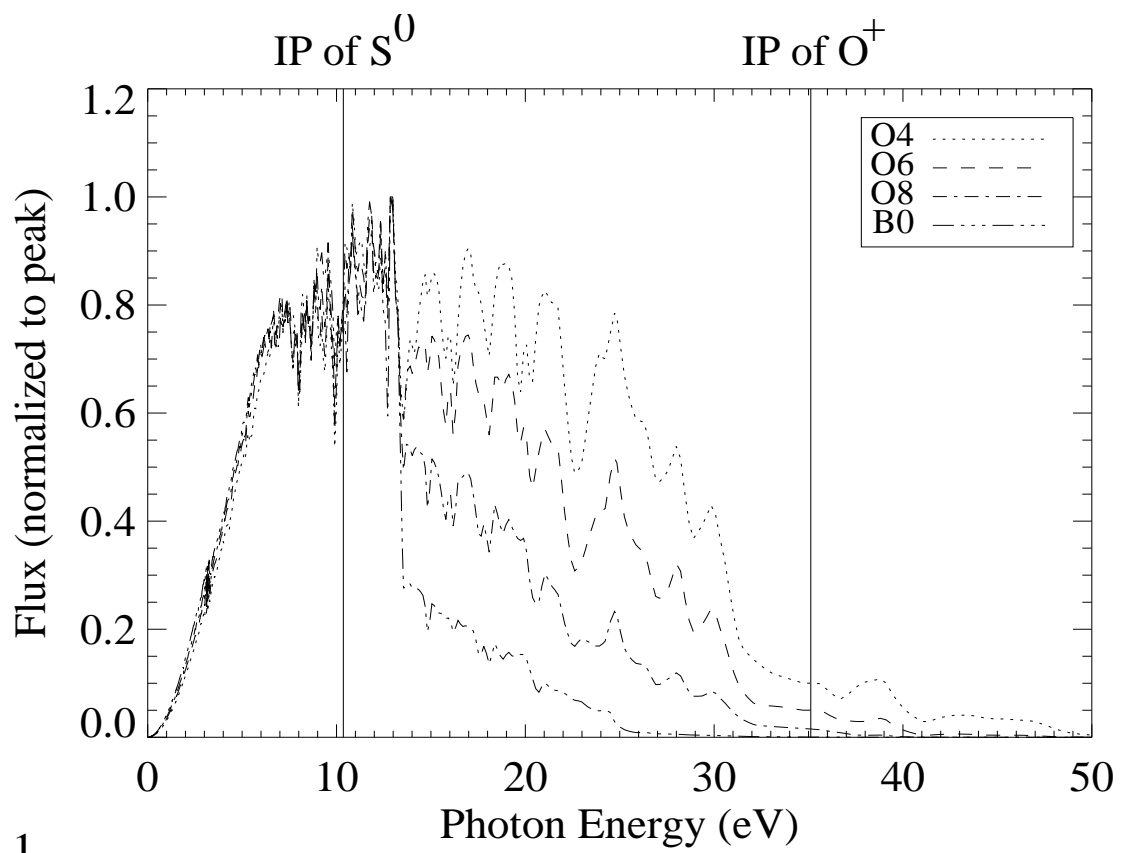


Fig. 1

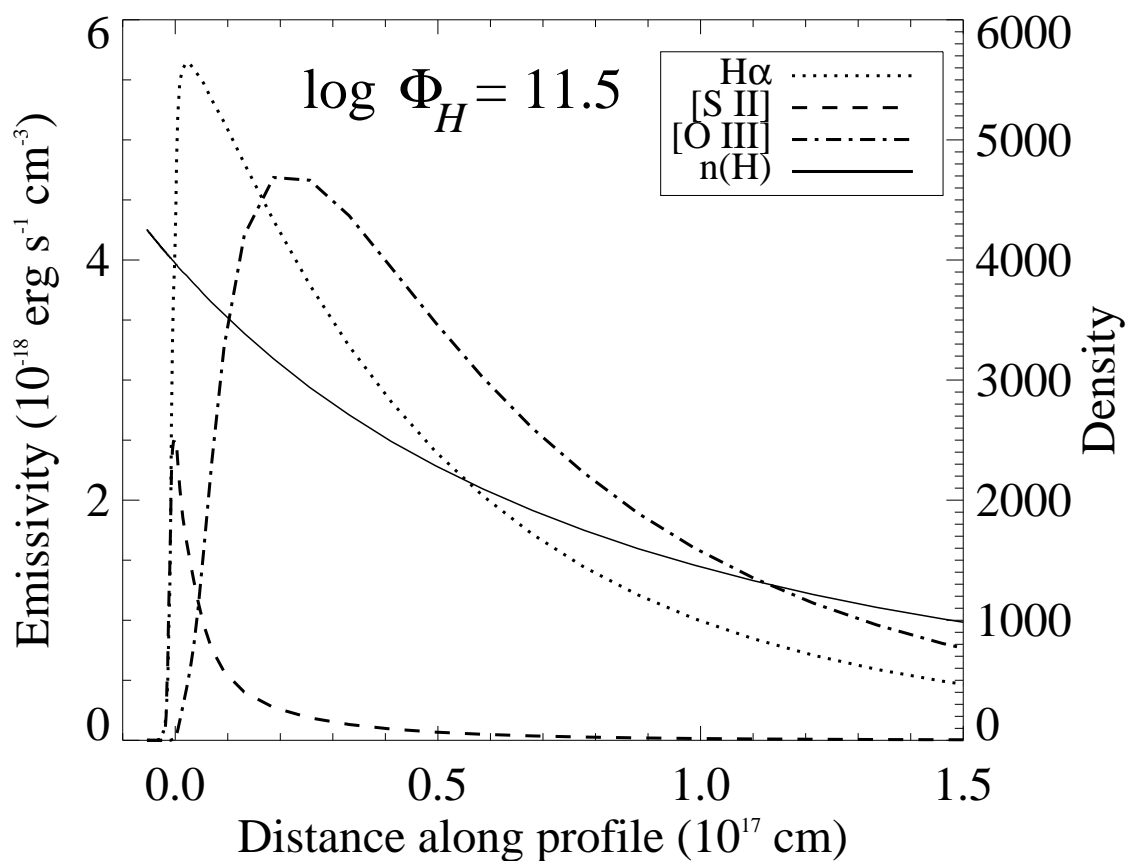
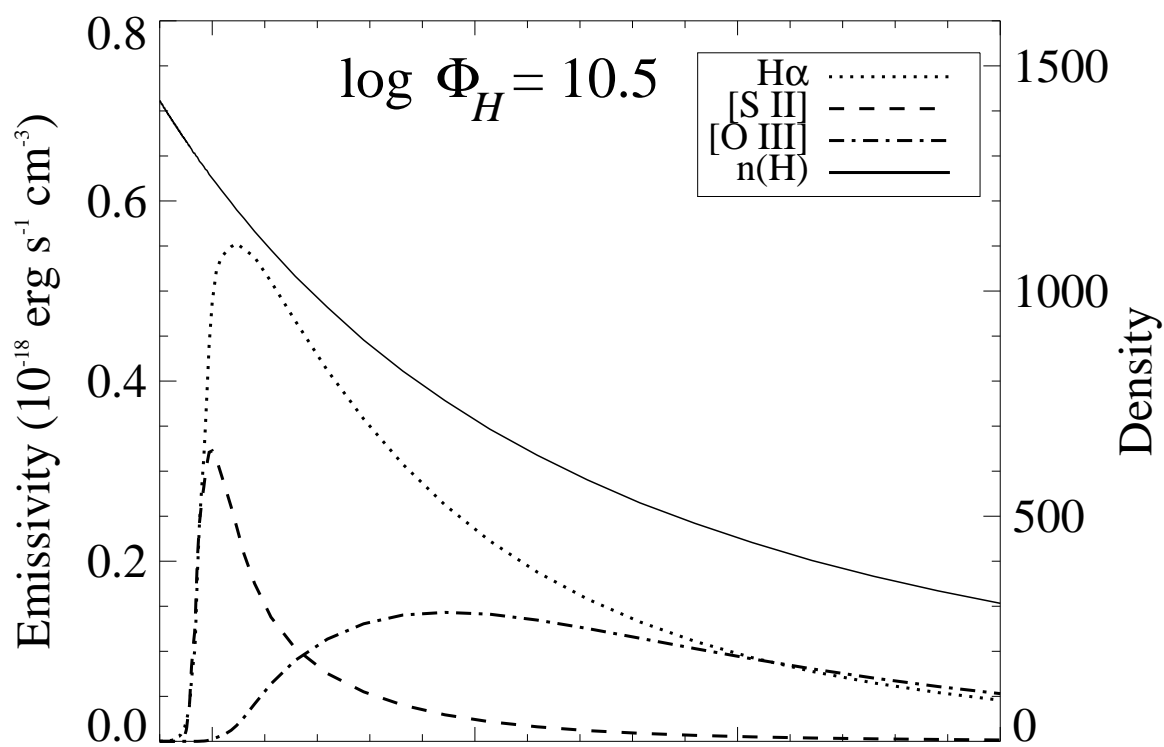


Fig. 2

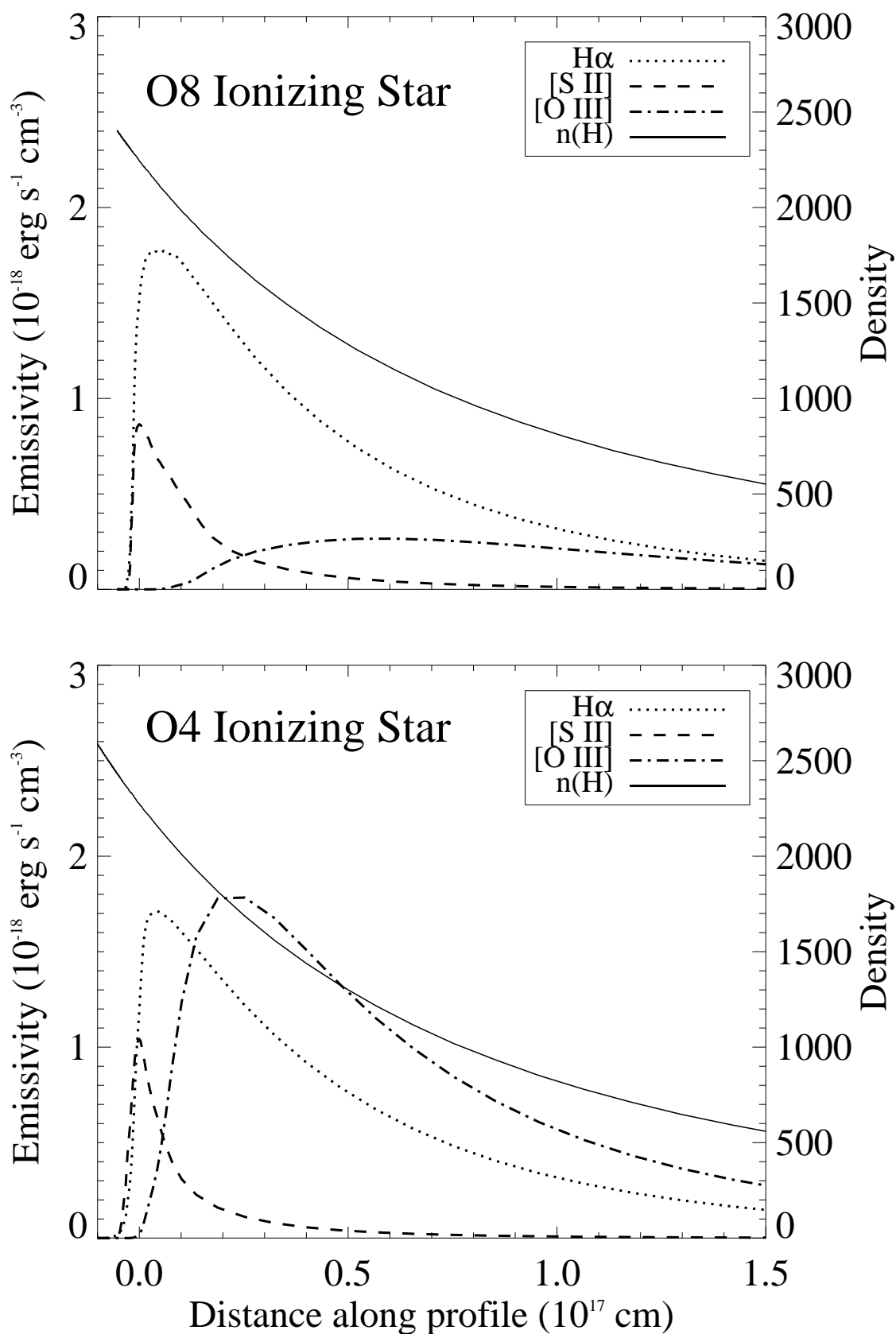


Fig. 3

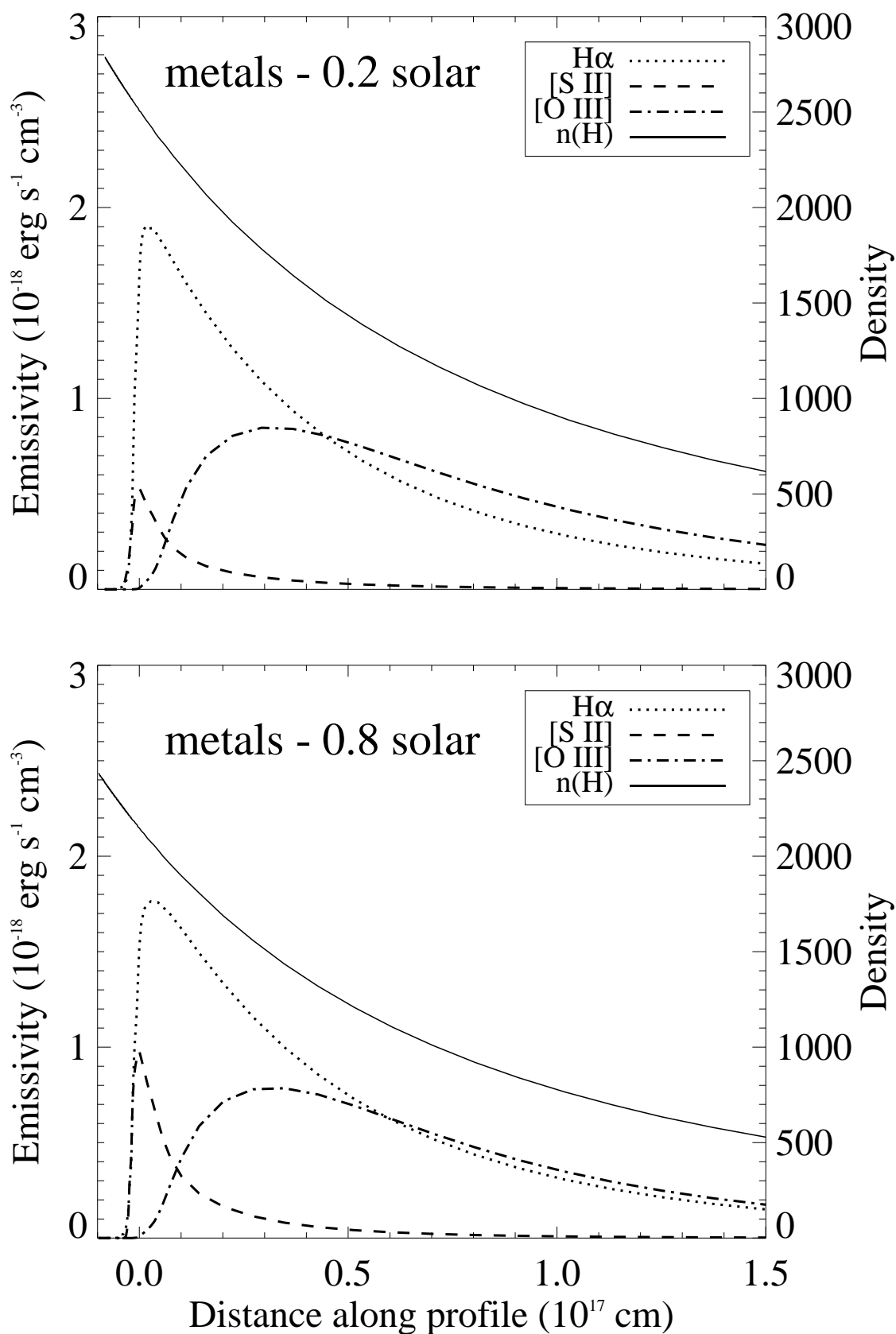


Fig. 4

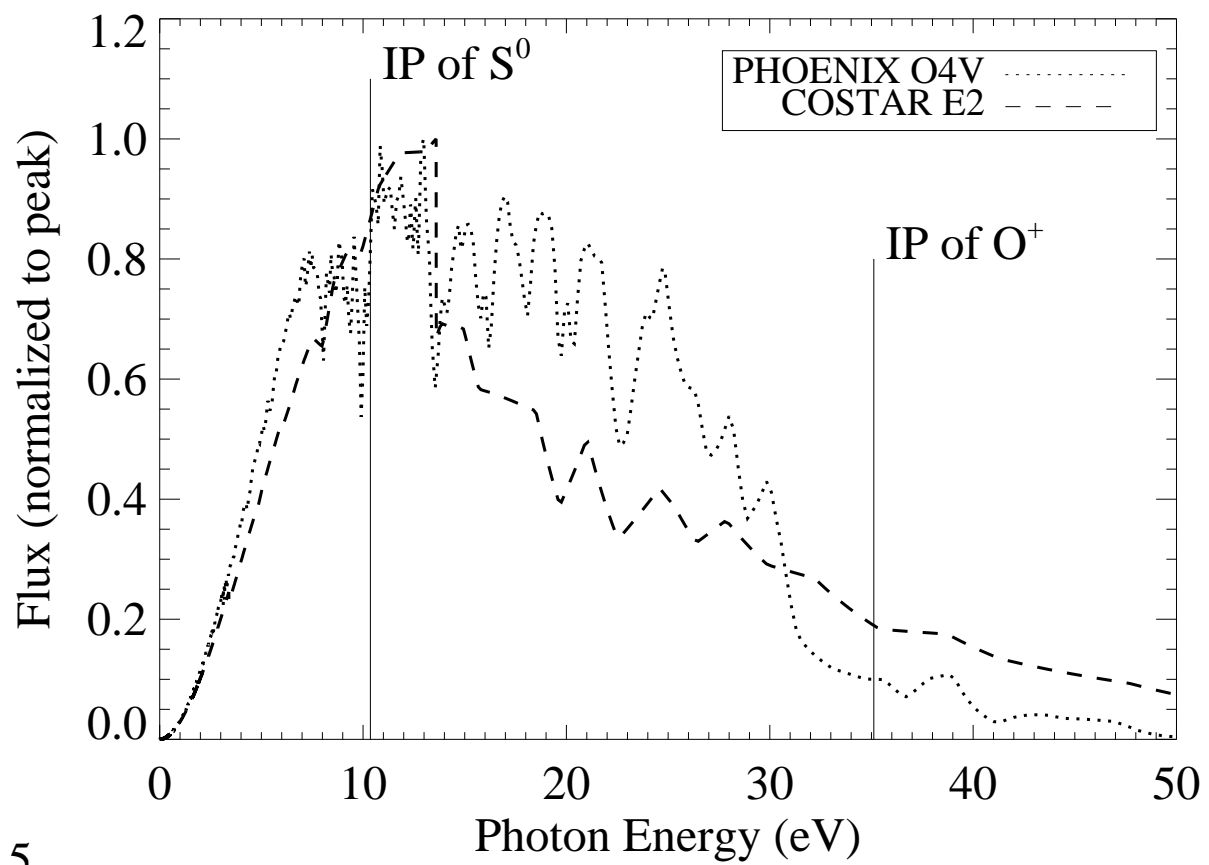


Fig. 5

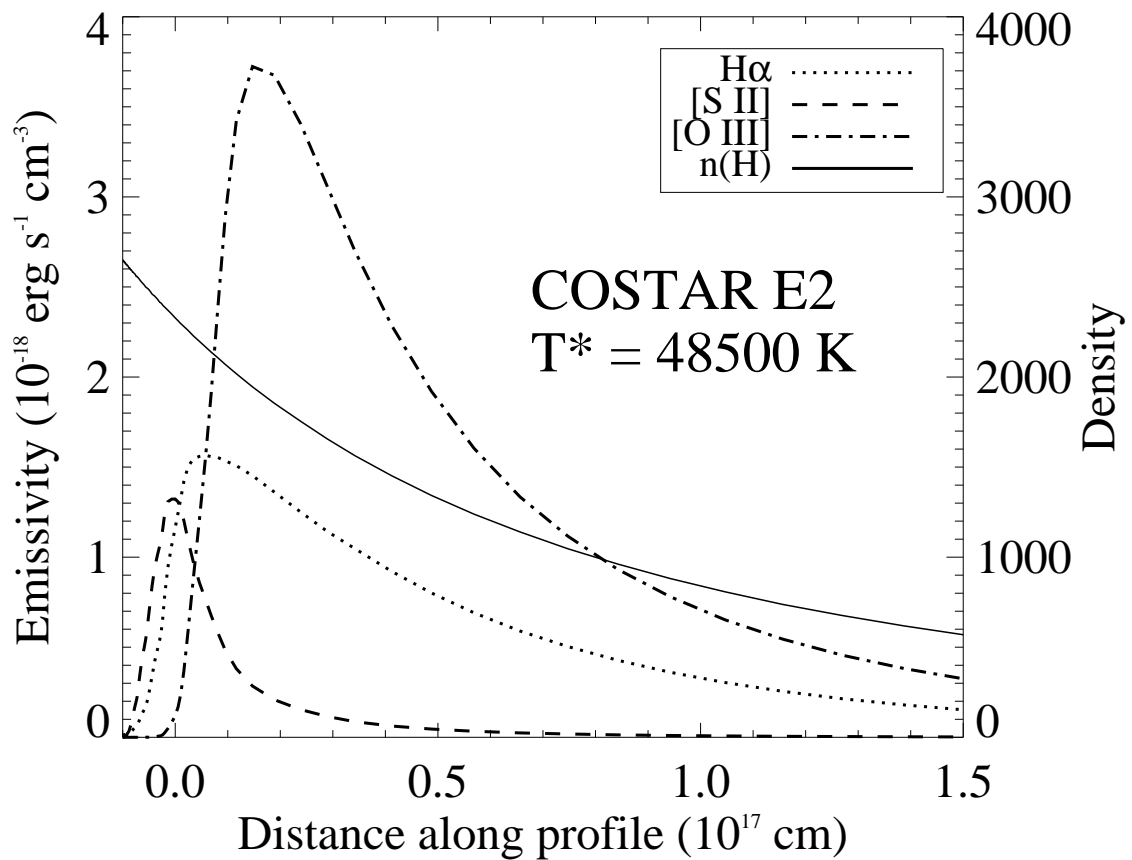
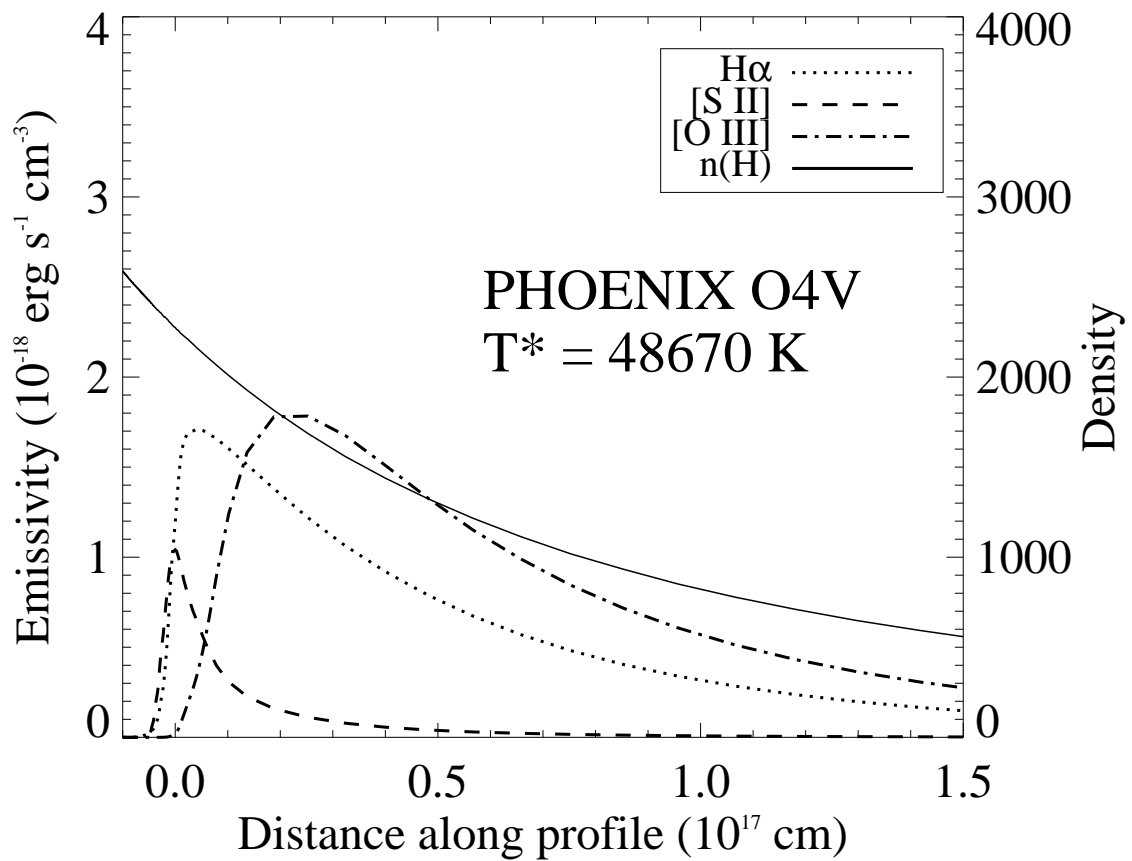


Fig. 6

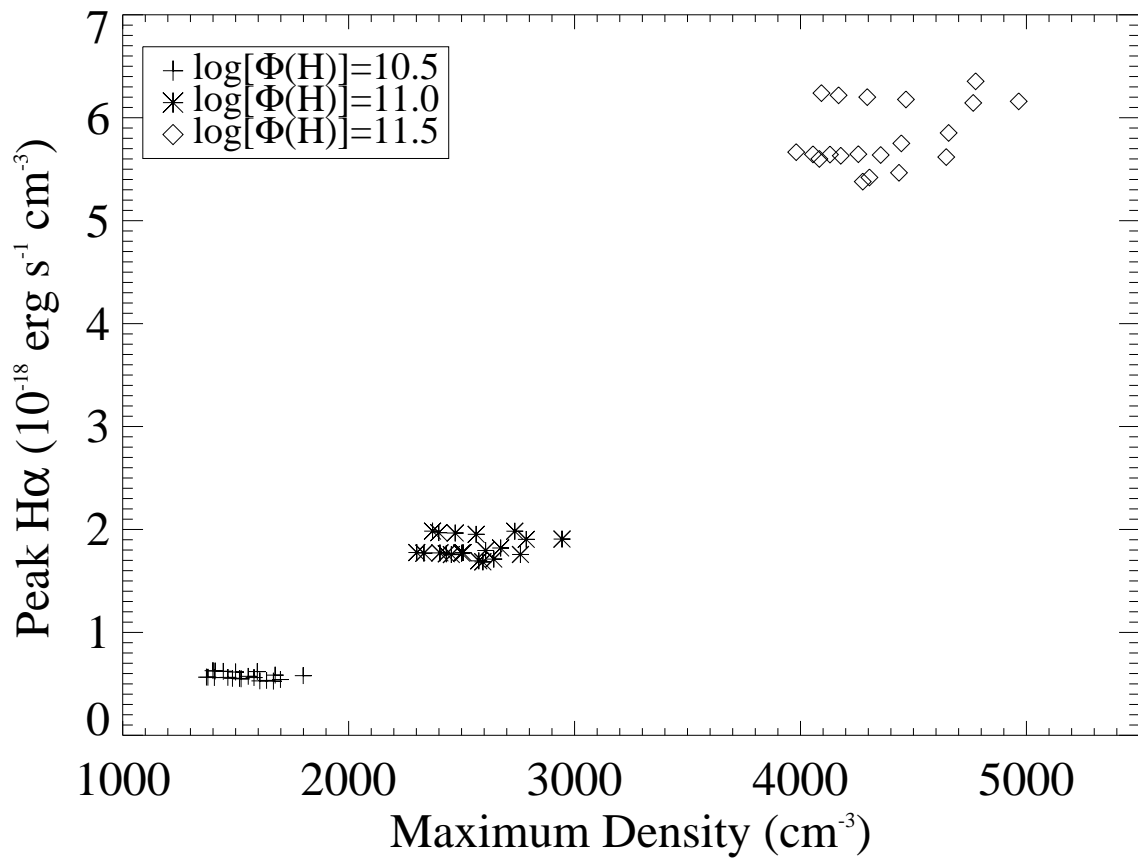
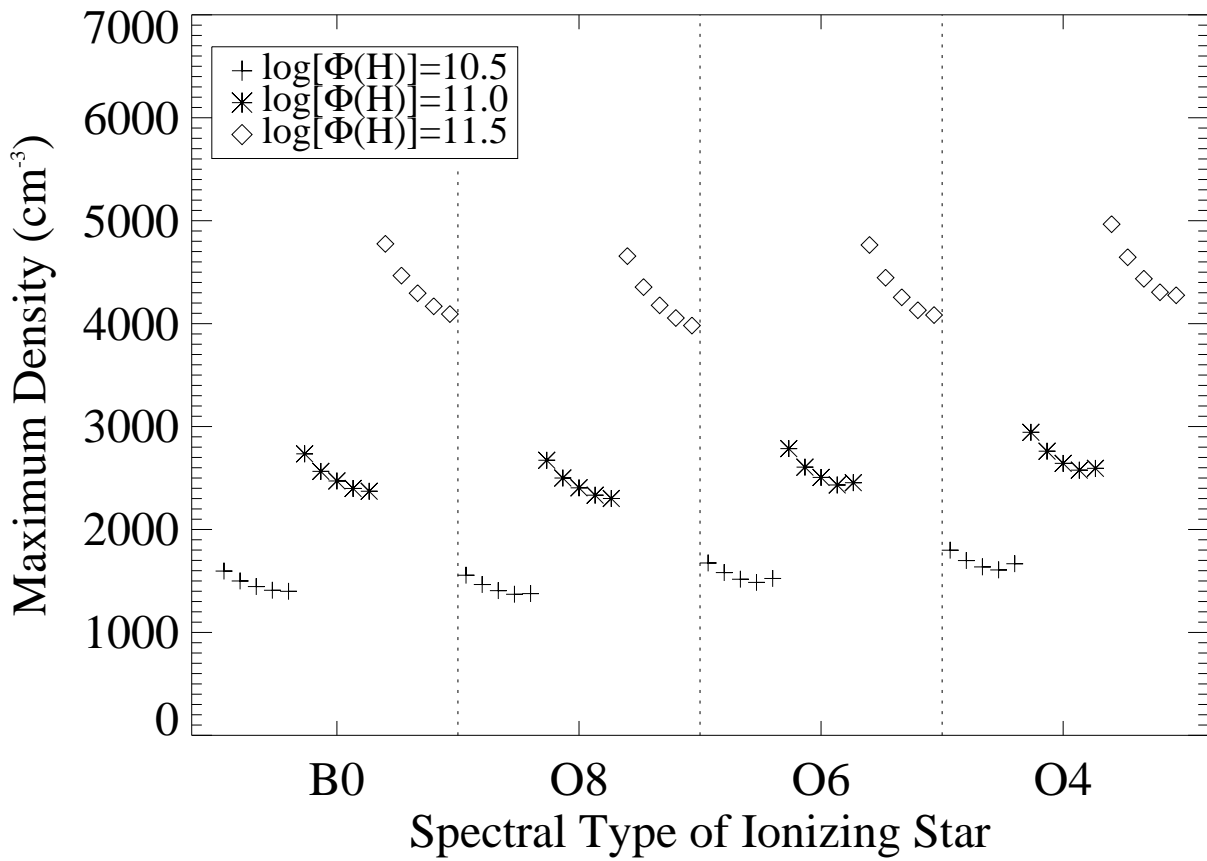


Fig. 7

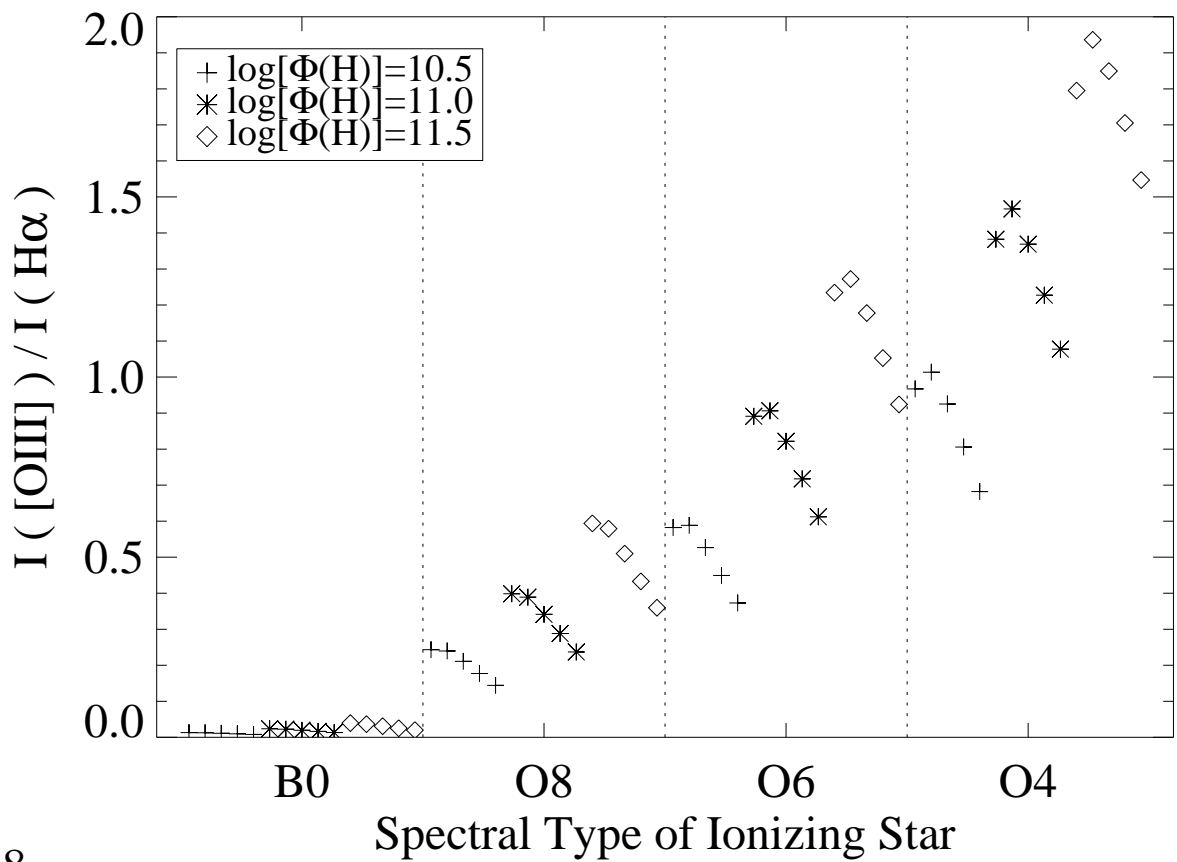
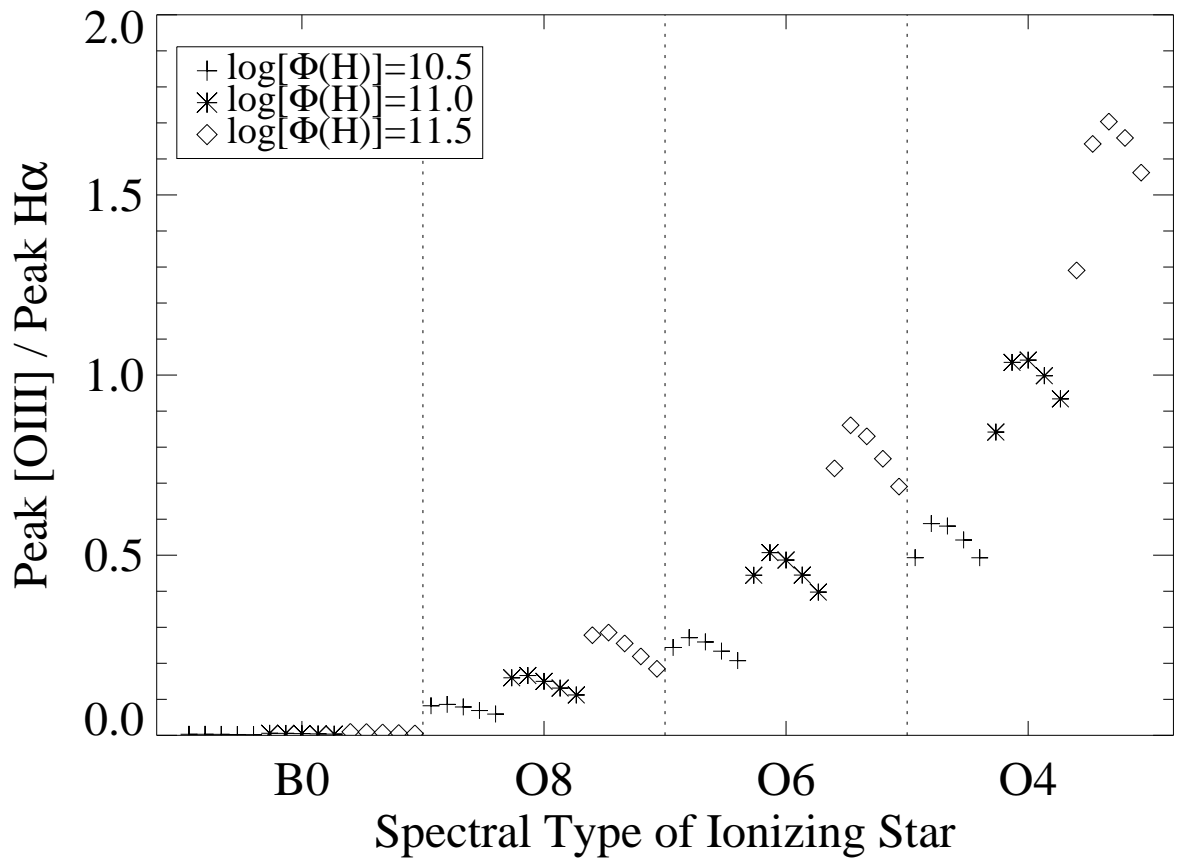


Fig. 8

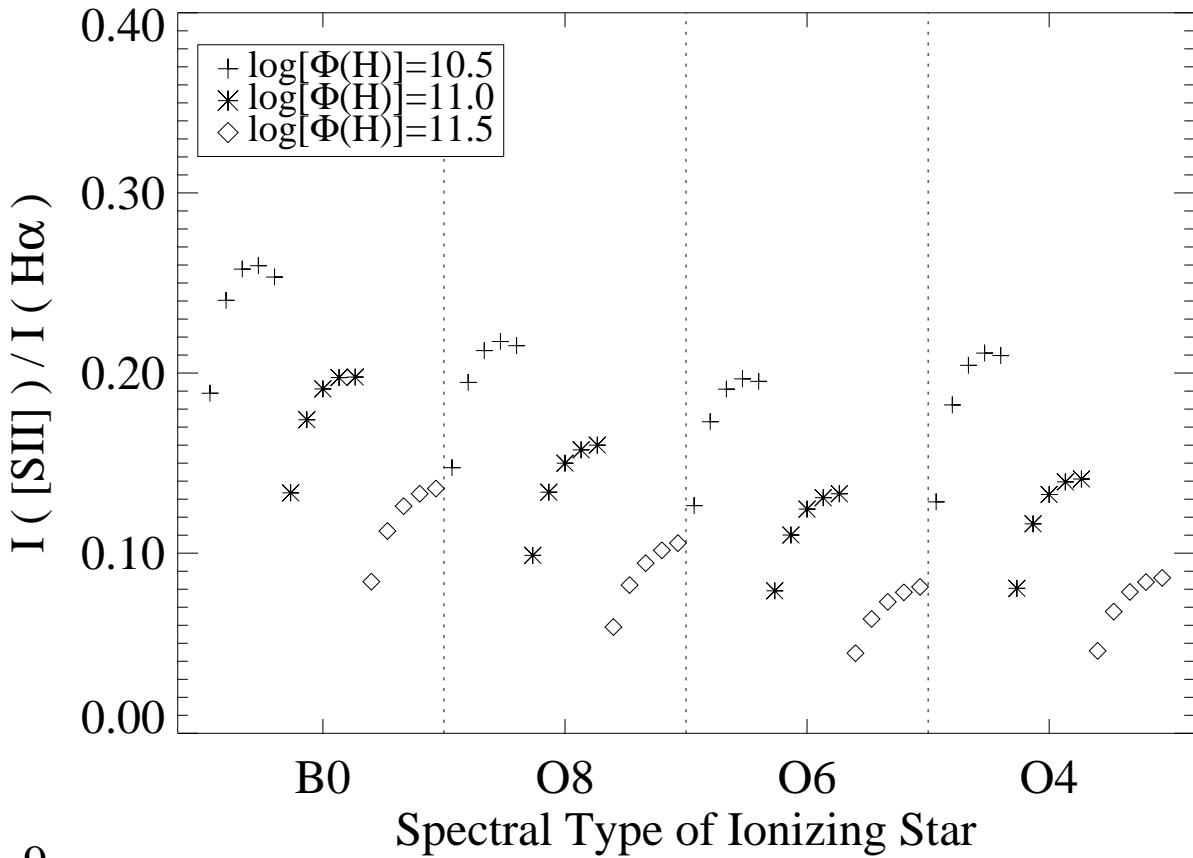
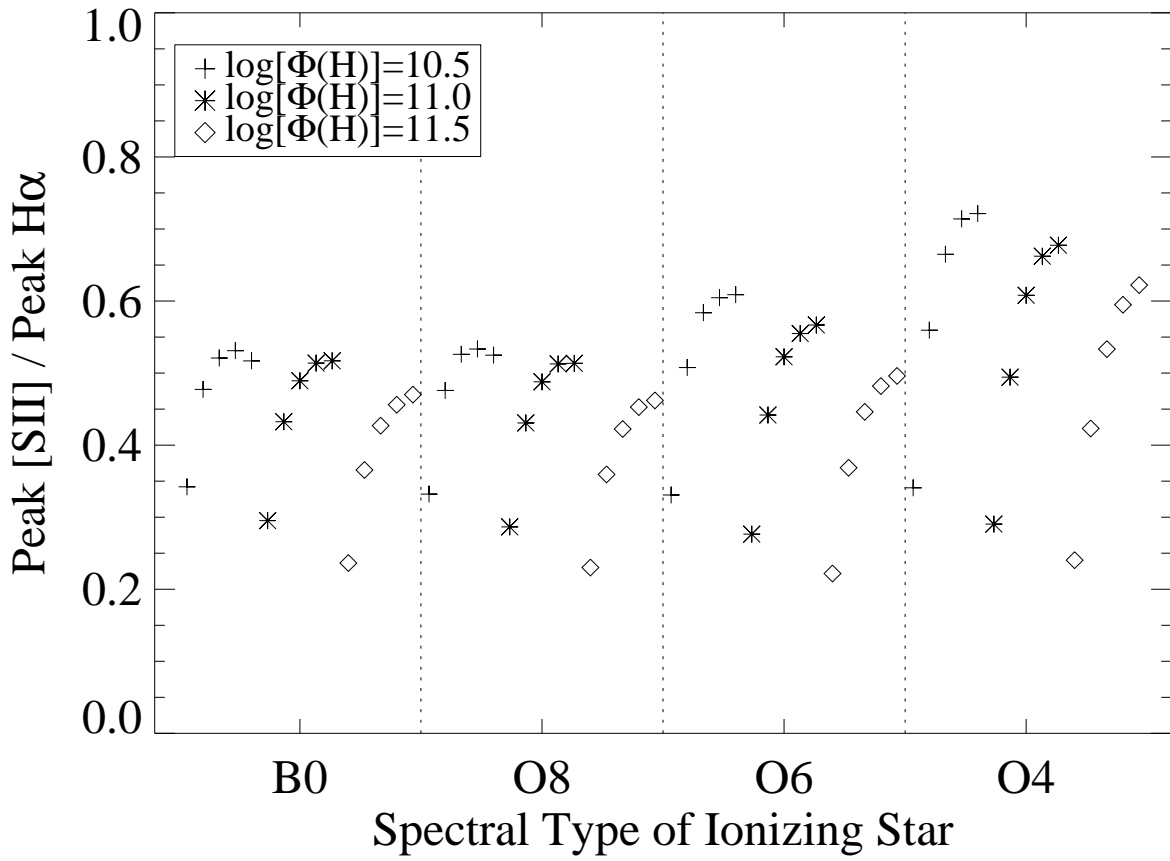


Fig. 9

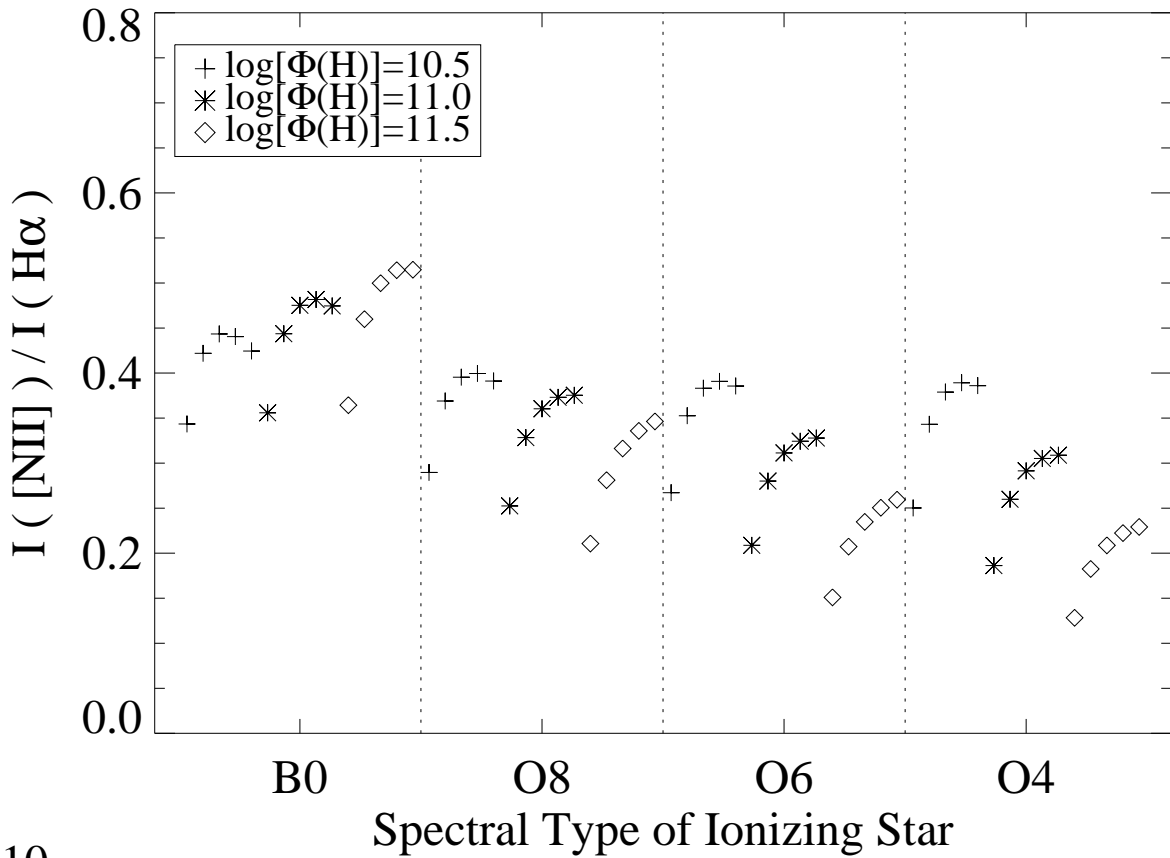
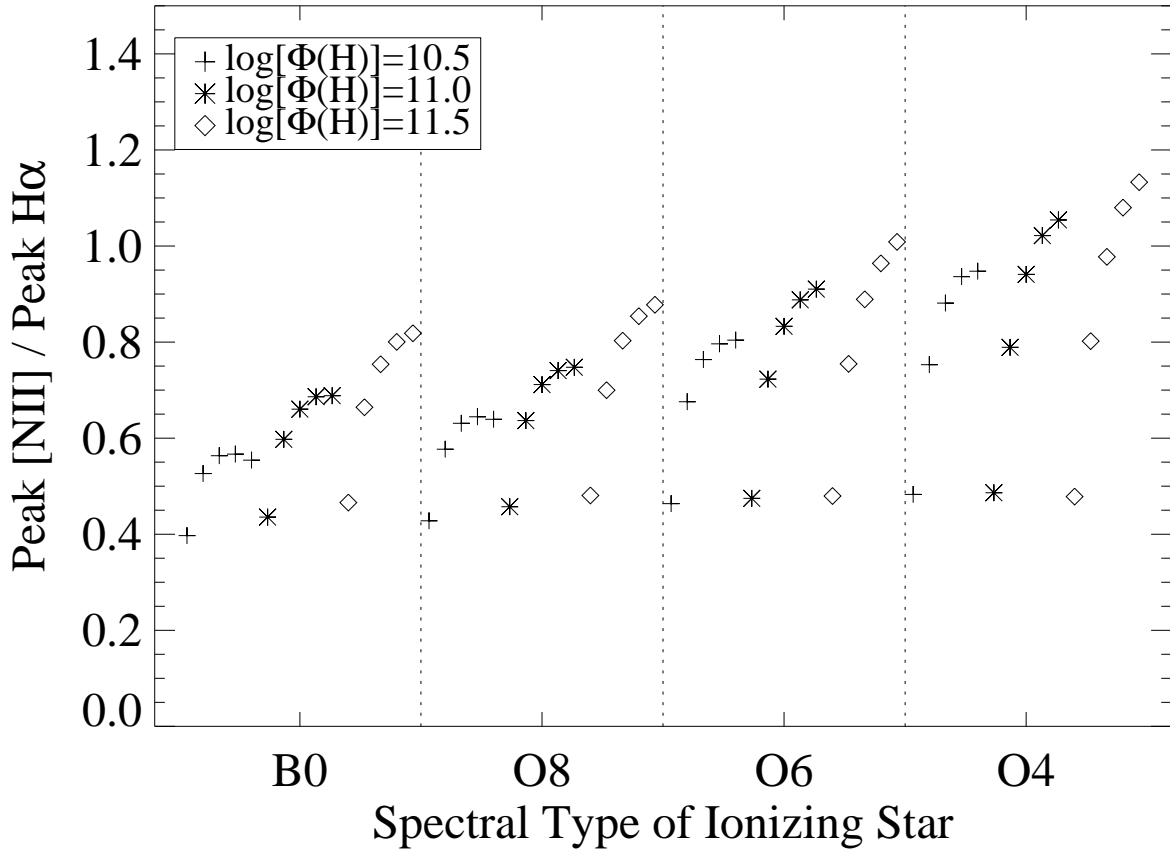


Fig. 10

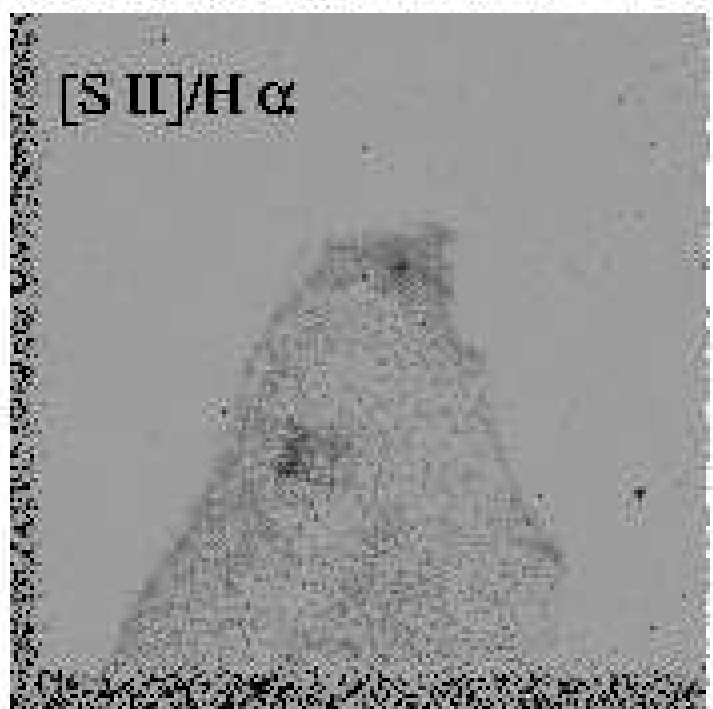
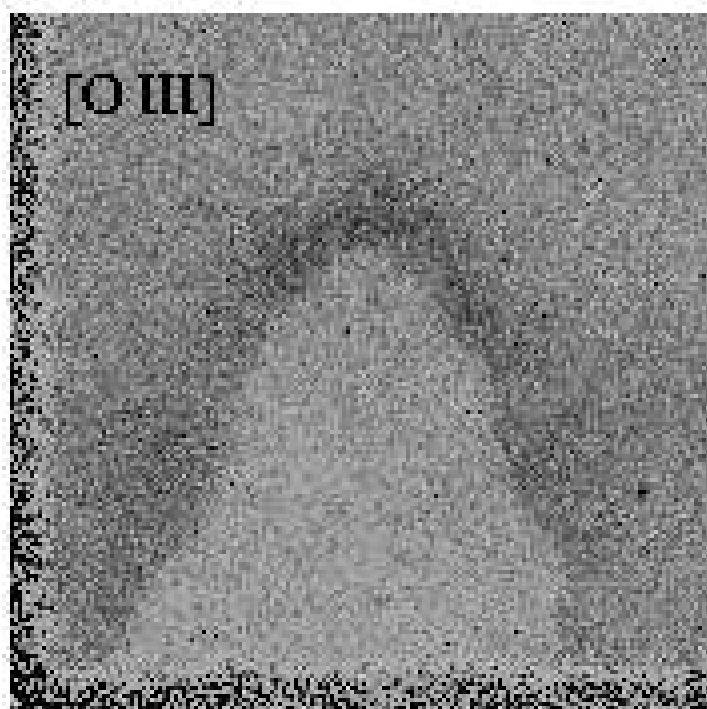
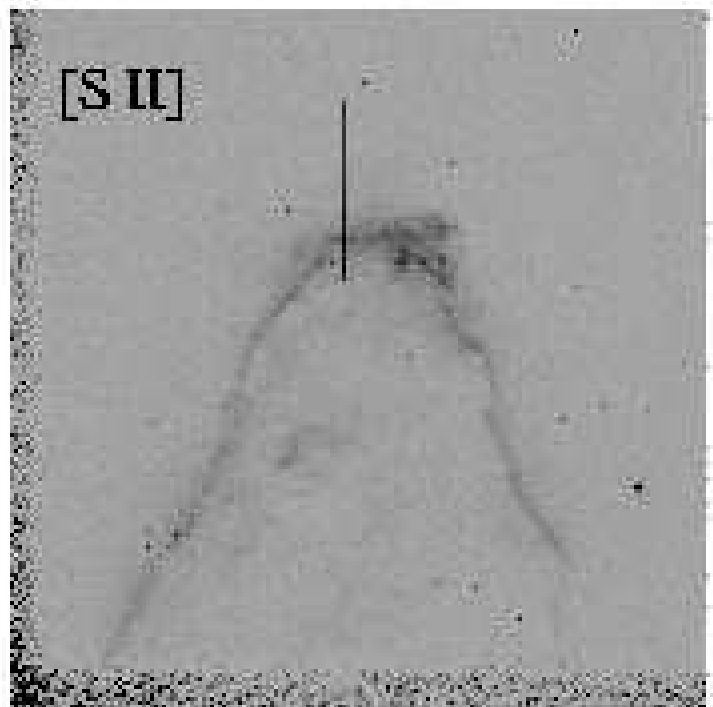
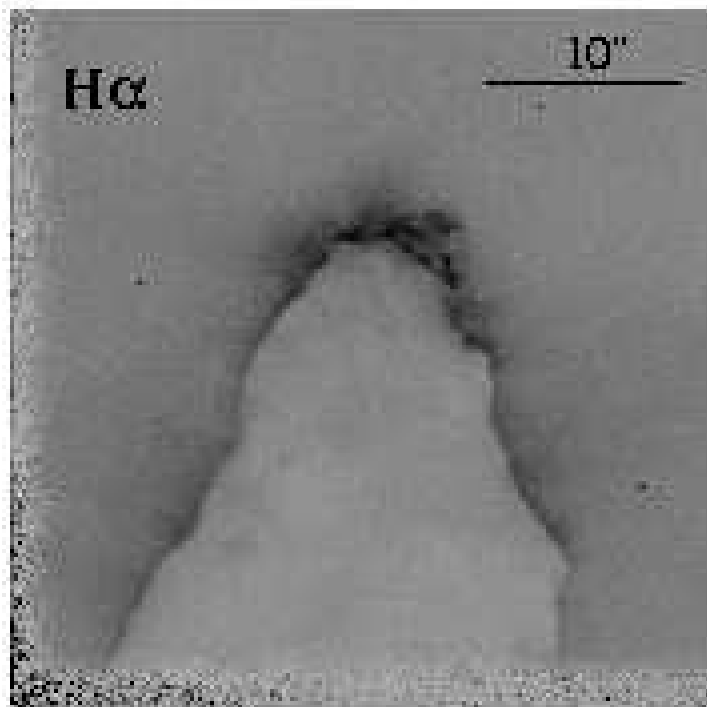


Fig. 11

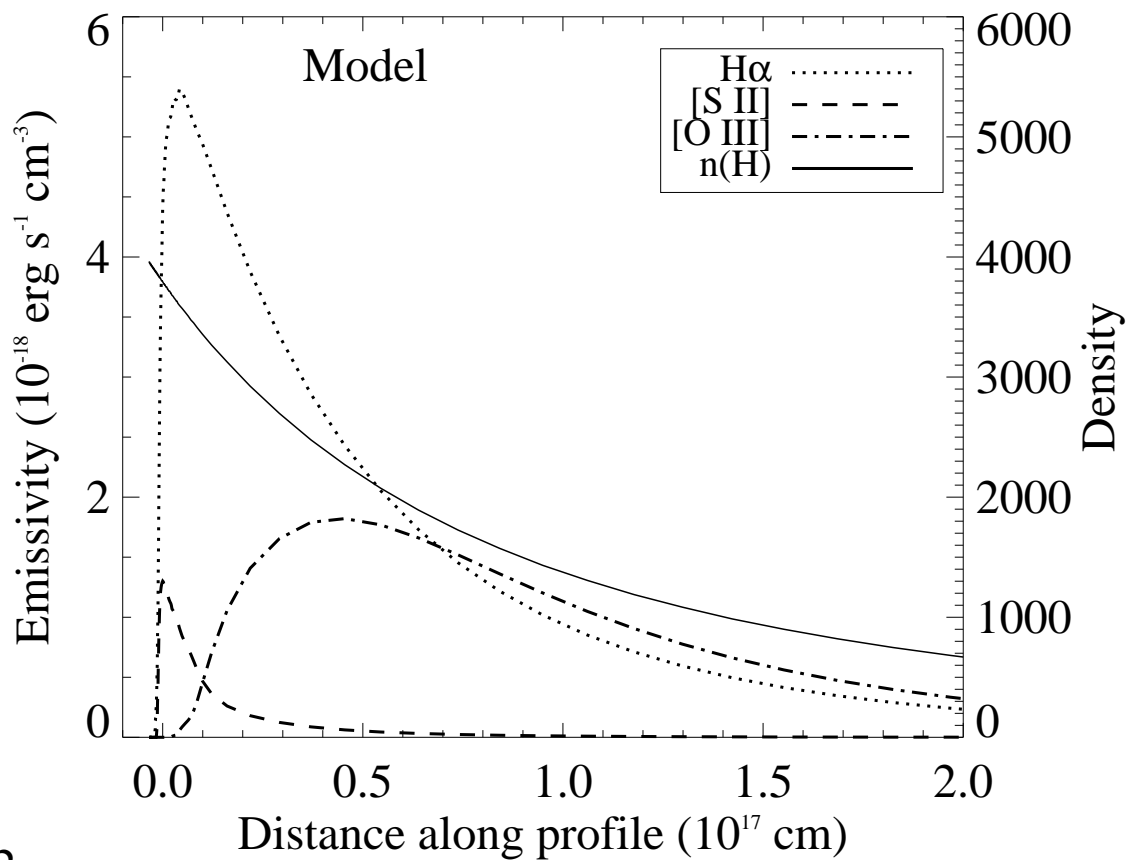
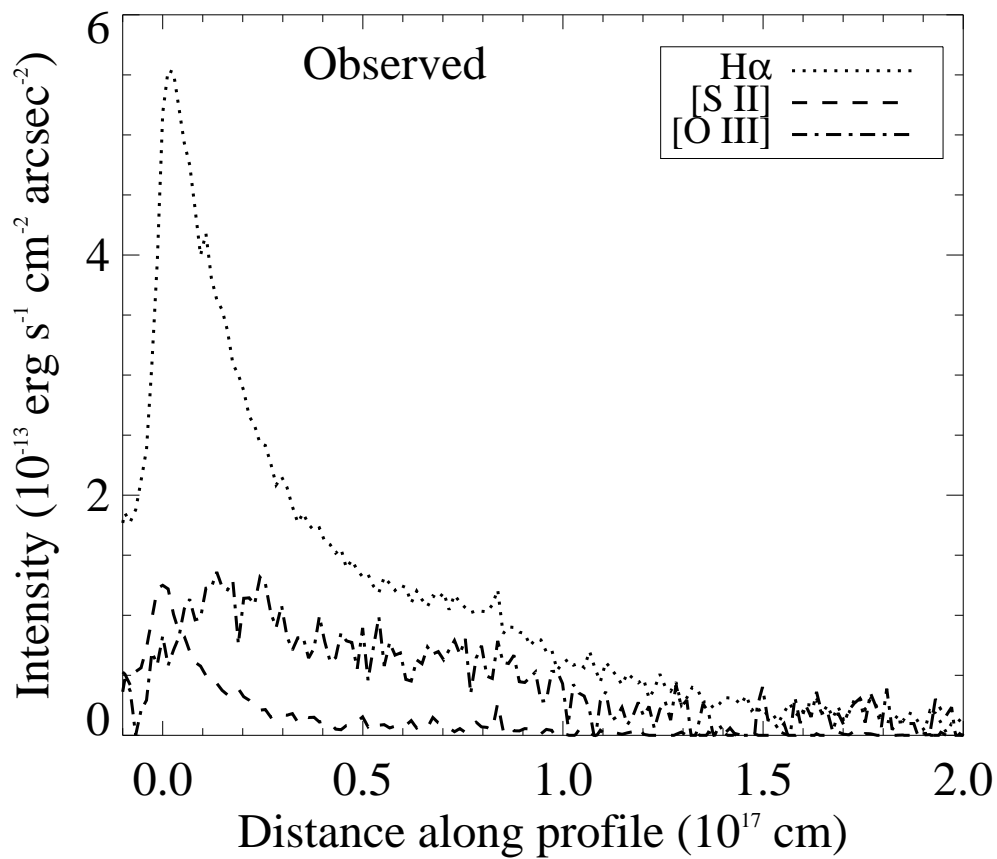


Fig. 12